Journal of Power Sources 264 (2014) 147–154

Contents lists available at ScienceDirect

Journal of Power Sources

journal homepage: www.elsevier.com/locate/jpowsour

Li_2ZrO_3-coated $0.4Li_2MnO_3 \cdot 0.6LiNi_{1/3}Co_{1/3}Mn_{1/3}O_2$ for high performance cathode material in lithium-ion battery

Xiaowei Miao [a,b], Huan Ni [a], Han Zhang [a], Chunguang Wang [a], Jianhui Fang [b], Gang Yang [a,*]

[a] Jiangsu Lab of Advanced Functional Material, Changshu Institute of Technology, Changshu 215500, China
[b] Department of Chemistry, Shanghai University, Shanghai 200444, China

HIGHLIGHTS

- Li_2ZrO_3 coating $0.4Li_2MnO_3 \cdot 0.6LiNi_{1/3}Co_{1/3}Mn_{1/3}O_2$ synthesized by sol–gel method.
- D_{Li+} of LMO increases one to two orders of magnitude after Li_2ZrO_3 coating.
- Li_2ZrO_3 coated sample delivers 263.7 mAh g^{-1} at 0.1 C and good cycle performance.
- Minor Li_2ZrO_3 modification enhances high-rate capability and cycle ability of LMO.

ARTICLE INFO

Article history:
Received 23 January 2014
Received in revised form
21 March 2014
Accepted 15 April 2014
Available online 26 April 2014

Keywords:
Lithium-ion batteries
Cathode materials
Coating
Electrochemical performance

ABSTRACT

To improve the high-rate capacity and cycle ability, minor Li_2ZrO_3 successfully coat the nanoparticles of $0.4Li_2MnO_3 \cdot 0.6LiNi_{1/3}Co_{1/3}Mn_{1/3}O_2$ (LMO) via sol–gel method. The crystal structure and electrochemical properties of the bare and coated material are studied by X-ray diffractometry (XRD), transmission electron microscopy (TEM), cyclic voltammetry (CV), galvanostatic intermittent titration technique (GITT), and charge–discharge tests. The lithium diffusion coefficient of LMO increases one to two orders of magnitude after Li_2ZrO_3 coating. Li_2ZrO_3 coating improves the rate capability and cycling stability of LMO. Within the cut-off voltage of 2.5–4.8 V, the initial discharge capacity of Li_2ZrO_3-coated $0.4Li_2MnO_3 \cdot 0.6LiNi_{1/3}Co_{1/3}Mn_{1/3}O_2$ (LZO-LMO) reaches to 264 mAh g^{-1} at 0.1 C rate, and the capacity remains 235 mAh g^{-1} after 100 cycles. At the current rates of 1, 2, 5 and 10 C, the maximum discharge capacities of LZO-LMO are 205.6, 161, 153.8 and 106 mAh g^{-1}, respectively. Minor Li_2ZrO_3 modification plays an important role to enhance the high-rate capability and cycle ability of LMO.

1. Introduction

The rechargeable lithium-ion batteries (LIBs) have been generally regarded as the energy storage for portable electric devices. Now it is expected to store and deliver higher energy and power to fulfill the requirements of electric vehicles (EVs), hybrid electric vehicles (HEVs) and plug-in hybrid electric vehicles (PHEVs) [1,2]. Cathode and anode materials building blocks determine the performance of LIBs. The capacity of the anode material is more than 300 mAh g^{-1} while that of the cathode is around 150 mAh g^{-1} [3,4]. The relatively lower capacity of the cathode materials, such as $LiCoO_2$, $LiMn_2O_4$, $LiFePO_4$, has become a bottleneck to improve the electrochemical performance of LIBs. Recently, lithium-rich Mn-based layered compounds, $Li_{1+x}[M]_{1-x}O_2$ or $xLi_2MnO_3 \cdot (1-x)LiMO_2$ (M = Ni, Co, Mn, $x > 0$), considered as cathode for LIBs [5,6], present the potential application due to their higher capacity (up to 250 mAh g^{-1}) and stability at higher cut-off voltage beyond 4.8 V [7,8]. In these compounds, Li_2MnO_3 and Li_2MnO_3-like domains exist with short-range order within $LiMO_2$ matrix [9]. The component of Li_2MnO_3 plays the role to enhance the discharge capacity of $xLi_2MnO_3 \cdot (1-x)LiMO_2$ by simultaneously extracting Li_2O at potential above 4.5 V, and stabilize the structure to facilitate the diffusion of Li^+-ion during charge/discharge process [5].

There are several drawbacks to limit the application of lithium-rich cathode in high power LIBs, for example, the severe capacity fading during cycling at high current rates [10,11]. The capacity fading is mainly related to the unstable structure while the cathode carries out beyond 4.8 V [12], and the poor rate performance is attributed to the low conductivity induced by Li_2MnO_3

* Corresponding author. Tel.: +86 512 52251895; fax: +86 512 52251842.
E-mail addresses: gangyang@ua.pt, gyang@cslg.edu.cn (G. Yang).

http://dx.doi.org/10.1016/j.jpowsour.2014.04.068
0378-7753/

component [11]. In order to resolve these problems, doping and coating are efficient strategies. Doping stabilizes the structure but causes a fading of capacity because the substituents are usually electrochemically inactive ingredients, such as Al, Mg, Zn, etc. [13]. Modification of the cathode material by coating a small amount of inert metal oxides, such as Al_2O_3, ZnO, V_2O_5, ZrO_2 etc. [14–18], can significantly improve the cyclic performance by avoiding the unwanted reactions on the surface. However, the inert metal oxides are often poor electronic and ionic conductors, which usually lead to a large irreversible capacity and poor rate performance [19]. Recently, some Li-contained oxides, such as $LiAlO_2$ [20] and $Li_{3x}La_{2/3-x}TiO_3$ [21], effectively enhance the electrochemical performance because they have good conductivity and also provide the tunnel for Li^+ transportation during charge/discharge processes [19–22].

In this present work, Li_2ZrO_3-coated $0.4Li_2MnO_3\cdot0.6LiNi_{1/3}Co_{1/3}Mn_{1/3}O_2$ (LZO-LMO) is prepared via a wet chemical method followed by high temperature heat-treatment. X-ray diffraction, scanning and transmission electron microscopy have been conducted to confirm the structure and surface morphology. The cyclic stability and rate performance of LZO-LMO are evaluated. Galvanostatic intermittent titration technique tests are carried out to investigate the improvement in the electrochemical properties of LZO-LMO. The diffusion coefficient of Li^+-ion (D_{Li}^{+}) obtained by GITT gives an explanation for the superior electrochemical performance of the coated cathode material.

2. Experimental

The sample of $0.4Li_2MnO_3\cdot0.6LiNi_{1/3}Co_{1/3}Mn_{1/3}O_2$ (LMO) was prepared by sol–gel method using citric acid as a chelating reagent. Stoichiometric amounts of $Ni(CH_3COO)_2\cdot4H_2O$, $Co(CH_3COO)_2\cdot H_2O$, $Mn(CH_3COO)_2\cdot4H_2O$ and $LiCH_3COO\cdot H_2O$ (5% excess) were dissolved in a certain amount of anhydrous ethanol. The dissolved solution was dropped to a continuously stirred ethanol solution of citric acid. The mixed solution was evaporated until a gel was obtained. The prepared gel was preheated in air at 450 °C for 8 h. The precursor was annealed in air at 900 °C for 24 h.

Li_2ZrO_3-coated $0.4Li_2MnO_3\cdot0.6LiNi_{1/3}Co_{1/3}Mn_{1/3}O_2$ (LZO-LMO) is synthesized as following steps. The intermediate of LMO is synthesized at 450 °C for 8 h. The preheated precursor of LMO is ball-milled and sifted, and ultrasonically dispersed in anhydrous ethanol. According to the content of Li_2ZrO_3 2 wt% to LMO, stoichiometric amounts of $Zr(NO_3)_4\cdot5H_2O$ and $CH_3COOLi\cdot2H_2O$ (5% excess) dissolved in anhydrous ethanol, are pumped into the suspension of LMO precursor at the speed of 6.0 mL min^{-1}. After continuous stirring at 75 °C, the as-produced gel is dried in vacuum. The mixture is heated at 650 °C for 5 h, and the final product LZO-LMO is produced at 900 °C for 24 h in air atmosphere. As comparison, the samples of LZO-LMO were synthesized according to the content of Li_2ZrO_3 1, 5 and 10 wt% to LMO, respectively.

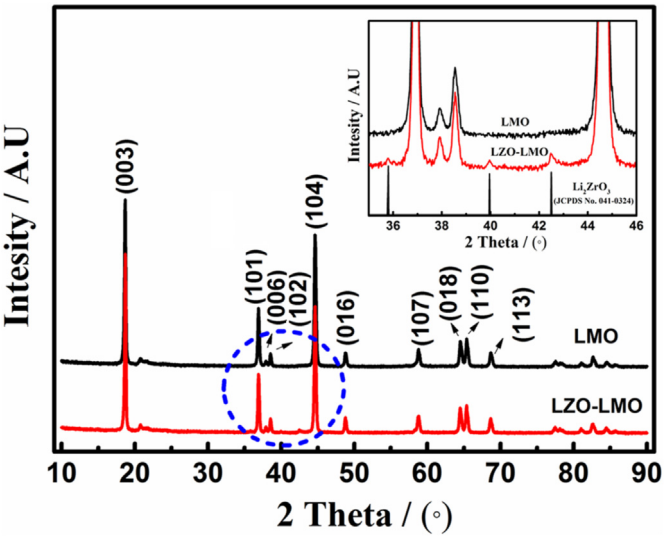

Fig. 1. X-ray diffraction patterns of LMO and LZO-LMO. Inset graph is magnified XRD patterns of LMO and LZO-LMO in the 2θ range of 35–46°.

Table 1
Lattice parameters from the Rietveld refinement of LMO and LZO-LMO.

Samples		LMO		LZO-LMO	
		LMO	LNCM	LMO	LNCM
Lattice parameters (Å)	*a*	4.9848	2.866	5.0058	2.8627
	b	8.5694	2.866	8.5635	2.8627
	c	5.0802	14.2924	5.0582	14.2763
	c/*a*	1.01	4.99	1.01	4.99
Lattice volume (Å^3)		204.65	101.66	204.52	101.32
Intensity ratio	$I_{(003/104)}$	1.26		1.41	
Reliability and	χ^2	3.606		2.09	
weighted factors	R_{wp}/(%)	10.06		7.59	
	R_P/(%)	7.67		6.03	

By using Rigaku diffractometer (D_{max}-2200) with Cu-Kα radiation, the X-ray diffraction patterns were collected at a scan rate of 2° min^{-1} from 10 to 90°. The crystal morphology was characterized by field-emission scanning electron microscope (FE-SEM, SIGMA, ZEISS microscope, 20 kV) coupled with an energy dispersive spectrum X-ray detector (EDS), and high-resolution transmission electron microscope (HRTEM, JEOL-2010F, 200 kV). Elemental composition (Li, Ni, Co and Mn) of the samples was measured by ICP-OES (Inductively Coupled Plasma Optical Emission Spectrometer, iCAP 6000). Specific surface areas were performed with a Micromeritics ASAP 2010 M + C nitrogen adsorption instrument (Micromeritics Inc., USA) at 77 K.

Electrochemical performances of the samples were collected in CR2016 coin cells. The positive electrodes of the active materials (80 wt%), Super P (10 wt%) and polyvinylidenefluoride (10 wt%) were mixed in *N*-methyl-2-pyrrolidone and stirred overnight. The slurry casted onto Al foil by using a doctor blade, and was dried at 120 °C for 12 h under vacuum. The material loading of the cathode electrode is 4–5 mg cm^{-2}, and the thickness of electrode is 80 μm. Cells were assembled in an argon-filled glove box by using lithium metal as the negative electrode, Celgard 2500 as the separator, and 1 M $LiPF_6$ dissolved in ethylene carbonate, dimethyl carbonate and ethyl-methyl carbonate with a 1:1:1 volume ratio as the electrolyte. The galvanostatic charge and discharge tests were made at ambient temperature by using LAND CT2001A battery testing system (Wuhan, China) within the voltage range of 2.5–4.8 V *vs.* Li^+/Li. Galvanostatic intermittent titration technique (GITT) was carried out at room temperature in the voltage range of 2.0–4.8 V. The electrochemical impedance spectroscopy (EIS) measurements were conducted on the PARSTAT2273 electrochemical workstation, and the amplitude of the input ac signal was kept at 5 mV, and the frequency range was set between 100 kHz and 0.01 Hz.

Table 2
The specific surface area and ICP analysis of LMO and LZO-LMO.

Samples	BET	Content (ppm)				Calculated molar ratio of Li:Ni:Co:Mn			
	(m^2 g^{-1})	Li	Ni	Co	Mn				
LMO	3.68	1.0000	1.2470	1.2010	3.4260	1.44	0.21	0.20	0.62
LZO-LMO	4.35	1.0020	1.2160	1.1520	3.2860	1.44	0.21	0.20	0.60

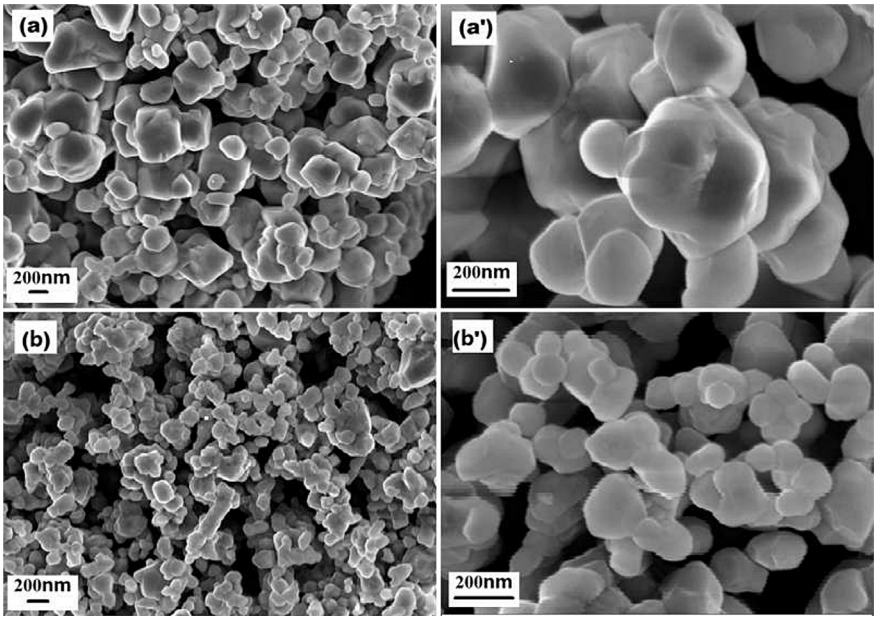

Fig. 2. SEM images of LMO (a) and (a′), and LZO-LMO (b) and (b′) with two magnifications.

3. Results and discussion

The XRD patterns of LMO and LZO-LMO are shown in Fig. 1. The samples have high crystallinity for the sharp diffraction peaks. The strong XRD peaks are well indexed based on the α-$NaFeO_2$ structure with *R-3m* space group. The weak peaks between 20 and 25° are indexed to monoclinic unit cell *C2/m* which superlattice peaks are consistent with the $LiMn_6$ arrangement occurred in transition metal layers of Li_2MnO_3 nano-domains [23]. The value of $I_{(003)}/I_{(104)}$ (>1.2) is an indicator of the disorder between Li and Ni cations [24]. Both LMO and LZO-LMO present low amount of disorder between lithium and transition metal cations, because the intensity ratios of $I_{(003)}/I_{(104)}$ of LMO and LZO-LMO are estimated 1.25 and 1.41, respectively. In addition, the splitting peaks at 64.6° (018) and 65.4° (110) are distinct which reflect the ordered structure of LMO before and after coating [25]. The existence of Li_2ZrO_3 doesn't interfere with the growth of layer structural $0.4Li_2MnO_3 \cdot 0.6LiNi_{1/3}Co_{1/3}Mn_{1/3}O_2$. As shown in the inset graph of Fig. 1, the minor diffraction peaks at 35.8°, 39.9° and 42.5° are identified as (112), (004) and (020) of Li_2ZrO_3 (JCPDS card No. 041-0324). This result suggests that Li_2ZrO_3 phase grows to coat $0.4Li_2MnO_3 \cdot 0.6LiNi_{1/3}Co_{1/3}Mn_{1/3}O_2$. Similar XRD patterns appear in LZO-LMO with various weight ratios of 1%, 5% and 10% (as shown in Fig. S1 in Supplementary Information), respectively.

The XRD patterns are refined by the Rietveld method with General Structure Analysis Software (GSAS Los Alamos National Laboratory, USA) and the refined lattice parameters are listed in Table 1. Because the complex structure of $xLi_2MnO_3 \cdot (1-x)LiNi_{1/}$

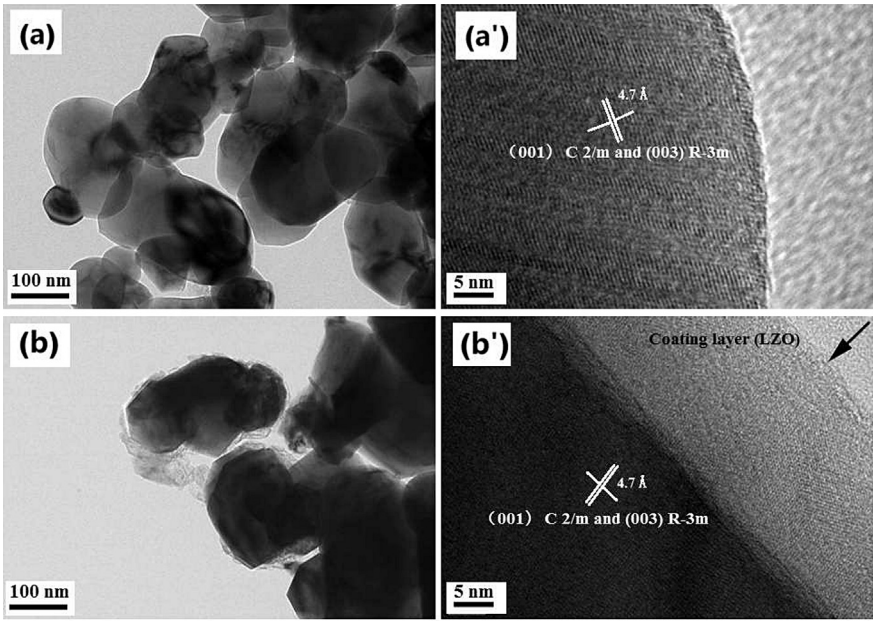

Fig. 3. TEM and HRTEM of LMO (a) and (a′), and LZO-LMO (b) and (b′).

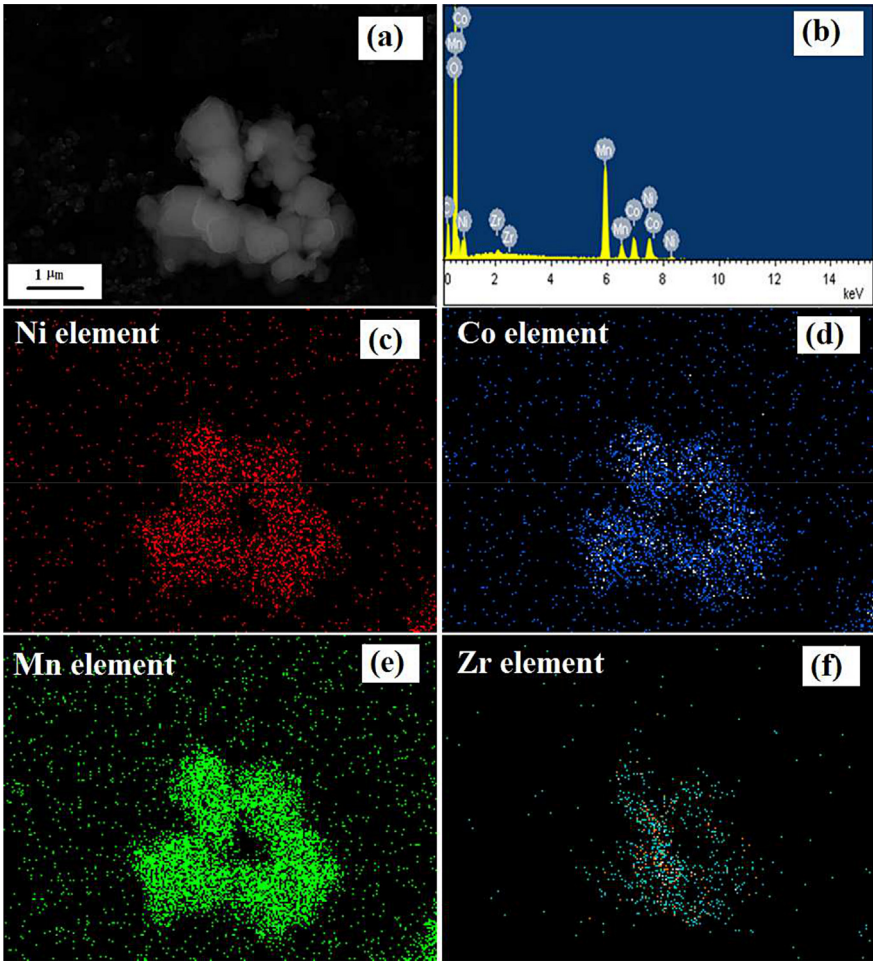

Fig. 4. SEM image of LZO-LMO (a), energy dispersive spectrum (b), and elemental mappings of Ni, Co, Mn and Zr (c, d, e, f).

$_3Co_{1/3}Mn_{1/3}O_2$ contains crystallographic sites shared by more than two cations, it is hard to obtain reliable results on atomic occupancies from the Rietveld refinement. In this work, the XRD diffraction patterns are refined by two sets of diffraction data: α-$NaFeO_2$ type with *R-3m* and monoclinic unit cell, *C2/m* characterized Li_2MnO_3. The reliability factor of χ^2 is less than 6, and the weighted factors of R_{wp}, R_p are less than 10%. As listed in Table 1, the cell parameters of LMO with and without Li_2ZrO_3 modification present minor change. For example, the cell parameter *a* by α-$NaFeO_2$ type with *R-3m* are 2.8660 and 2.8627 Å in LMO and LZO-LMO, and the lattice volumes are 204.65 and 204.52 $Å^3$, respectively. The almost same values of *c*/*a* and cell volume indicate the lattice structure of LMO still remains before and after Li_2ZrO_3 coating.

The atomic compositions of LMO and LZO-LMO are listed in Table 2. The molar ratios experimentally determined for Li, Ni, Co and Mn elements are very close to the stoichiometric values of 1.4:0.2:0.2:0.6 except that the Li is minor excess. As listed in Table 2, the BET specific surface area of LMO and LZO-LMO are 3.68 and 4.35 $m^2\ g^{-1}$, respectively. Both LMO and LZO-LMO samples have impact morphology which is important for the volume energy density as cathode for LIBs.

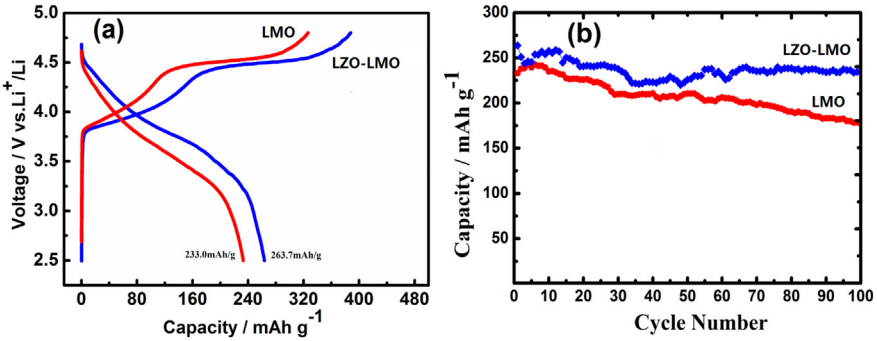

Fig. 5. Initial charge/discharge profiles (a) and cycling performance (b) of LMO and LZO-LMO as cathode carried out in the voltage range of 2.5–4.8 V at 0.1 C.

Fig. 2 shows the SEM images of LMO and LZO-LMO. Both samples are high crystallinity and homogeneous without obvious aggregation. The particle size of LMO decreases a little after Li_2ZrO_3 coating. As shown the SEM images with large magnification in Fig. 2a′ and b′, the estimated particle sizes of LMO and LZO-LMO are 300 and 220 nm, respectively. The TEM and HRTEM images of LMO and LZO-LMO powders are shown in Fig. 3. The surface of pure LMO particles is smooth and there is no other impurity phase on the surface of particles. Fig. 3b′ shows a coating layer on the surface of LMO particles. The calculated distance between two lattice fringes of LMO and LZO-LMO is both 4.7 Å, corresponding to (003) plane of the hexagonal layered phase $LiMO_2$ or (001) planes of monoclinic Li_2MnO_3-like component [26,27]. The crystal structure of LMO is the same with or without Li_2ZrO_3 coating. As shown in Fig. 3b′, a homogeneous coating layer of Li_2ZrO_3 grows on the surface of LMO, and the thickness of LZO layer is estimated about 15 nm. The functions of LZO-coated LMO include that LMO plays the role of energy storage/delivery and LZO as the bridge to improve the diffusion ability between the bulk of LMO and electrolyte [18,19].

The atomic compositions and elemental mapping of LZO-LMO are evaluated by EDS analysis and shown in Fig. 4. The atomic ratio of Mn:Co:Ni in pure LMO is nearly 3.07:0.998:1.00 (the images are not shown here) close to the theoretical value of 3:1:1, and that of Mn:Co:Ni:Zr in LZO-LMO is 2.73:0.882:1.00:0.0675, close to the theoretical value of 3:1:1:0.0683. As shown in Fig. 4c–f, the elemental distribution of LZO-LMO depends on the composition as well as the nanoscale spatial uniformity of transition metal elements. The EDS dot mapping (Fig. 4f) shows that the element of Zr in LZO-LMO is homogeneously distributed on the surface of LMO particles.

Fig. 5 shows the initial charge/discharge curves and cycle performance of LMO and LZO-LMO. Compared with the values of LZO-LMO (2 wt% of Li_2ZrO_3), the samples of LZO-LMO with 1, 5 and 10 wt % of Li_2ZrO_3 present poor electrochemical performance (as shown in Fig. S2 in Supplementary Information), and thus does not show here. The initial discharge capacities of LMO and LZO-LMO are 233 and 264 mAh g^{-1}, respectively. Both the materials exhibit two plateaus during the first charge process, located at 3.7–4.5 V and above 4.5 V. The first plateau is attributed to lithium-ion extraction from $LiNi_{1/3}Co_{1/3}Mn_{1/3}O_2$ phase corresponding to the oxidation of $Ni^{2+} \rightarrow Ni^{4+}$ and $Co^{3+} \rightarrow Co^{4+}$ [28]. The second plateau is considered to be the Li_2O taking off from the layered Li_2MnO_3 structure, which results in a high irreversible charge capacity [29]. For example, the initial charge and discharge capacities of LZO-LMO are 327 and 230 mAh g^{-1} in LMO, 388 and 264 mAh g^{-1}, respectively. With respect to the cycling performance (Fig. 5b), it can be observed that the capacity of LMO drops to 177 mAh g^{-1} after 100 cycles at 0.1 C, with capacity retention ratio of 77%. But LZO-LMO remains 235 mAh g^{-1} after 100 cycles, with 89% of the initial capacity. The introducing Zr element with appropriate ratio of 2 wt% successfully improves the structural stability and electrochemical properties of LMO. Based on the previous publications, the coating layer of Zr-contained materials on the surface of cathode can prevent the direct contact of electrode from electrolyte, therefore suppress the undesirable side reaction between them and the dissolution of transition metal ions caused by F-contained electrolyte [3,18].

The potential profiles of cycling between 2.5 and 4.8 V and the corresponding differential capacities *vs.* voltage plots are shown in Fig. 6. During the initial cycle, both the electrodes exhibit two couples of *dQ*/*dV* peaks, one at about 3.9 V and the other at about 4.6 V (*vs.* Li/Li^+). The peak at 3.9 V is ascribed to the extraction of Li^+ from $LiMO_2$ (M = Ni, Co, Mn) [28]. The peak at ~4.5 V is the irreversible reaction in which Li^+ is extracted from component

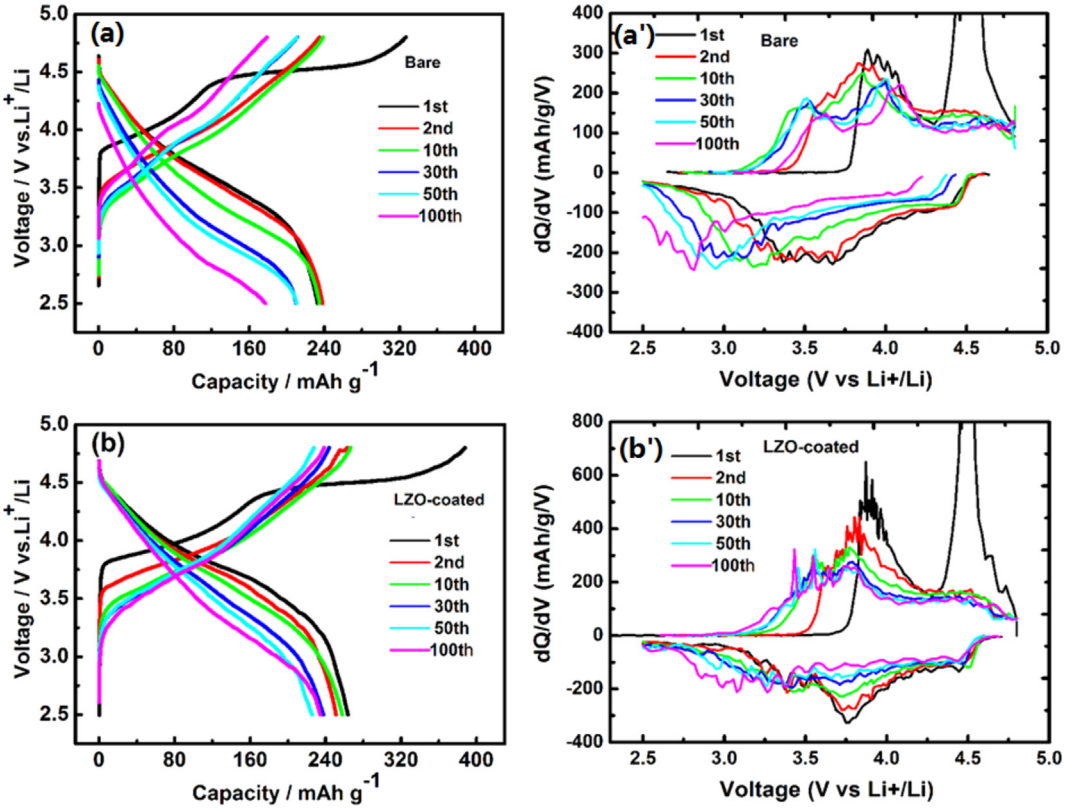

Fig. 6. The voltage profiles of LMO (a) and LZO-LMO (b) at the 1st, 2nd, 10th, 30th, 50th and 100th cycle, and the corresponding differential capacities *vs.* voltage plots (a′) and (b′).

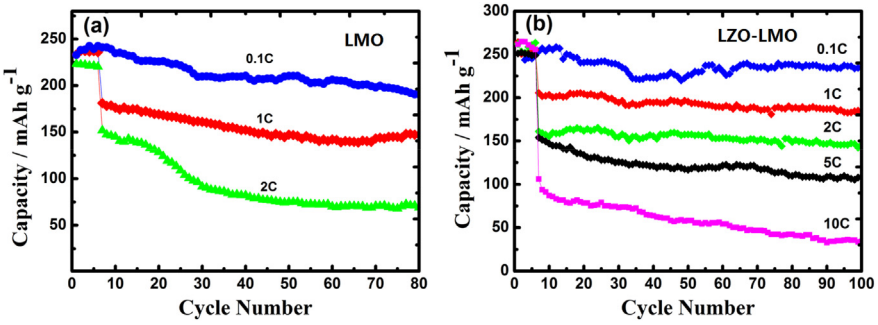

Fig. 7. High-rate cycling performances of LMO (a) and LZO-LMO (b). The batteries are charged/discharged for 5 cycles at 0.1 C before discharge at each high current density.

accompanying with the simultaneous release of oxygen [29]. At the second cycle, the anodic peak at ~4.5 V disappears, and the anodic peak at 3.9 V shifts to ~3.8 V. As the number of cycle increases, the dQ/dV peaks show slightly shifts and result in the different potential interval (ΔV) between the anodic and cathodic peaks. For example, at the 100th cycle the cathodic peak of LMO shifts to lower voltage of ~2.8 V than ~3.2 V in LZO-LMO. ΔV is representative of the kinetic process, especially considering that the electrochemical process involves lithium diffusion in a solid phase and electron jumping across the electrode materials. During 100 cycles, the ΔV of LZO-LMO present smaller values compared with those of LMO. The smaller ΔV of LZO-LMO is attributed to the coating of Li_2ZrO_3 which improves the extraction/reinsertion ability of lithium ions across the interface between the cathode of LMO and the electrolyte.

The rate performance of LMO and LZO-LMO is presented in Fig. 7 within the cut-off voltages of 2.5 and 4.8 V. The batteries are charged/discharged for 5 cycles at 0.1 C before carrying out at high current densities. The cathode LZO-LMO is discharged at 0.1, 1, 2, 5 and 10 C-rate, respectively, but LMO only shows the rate performance at 0.1, 1 and 2 C because of none response beyond the current rate of 5 C (Fig. 7a). Both LMO and LZO-LMO present the dropped capacities along with the increased discharge current densities. LMO delivers the initial capacities of 235, 181 and 152 mAh g^{-1}, lower than the values 253, 205.6, 161 of LZO-LMO at 0.1, 1 and 2 C-rate, respectively. Moreover, LZO-LMO delivers 154 and 106 mAh g^{-1} at high rates of 5 and 10 C. Li_2ZrO_3 coating on LMO greatly improves the cycle ability beside the rate capacity. For example, at 2 C-rate LMO presents rapid capacity fading, 152 mAh g^{-1} at the 5th cycle and only remaining 69 mAh g^{-1} after 80 cycles, but LZO-LMO delivers 161 mAh g^{-1} at the 5th cycle and remains 149 mAh g^{-1} after 100 cycles. Based on the previous publications, the thin layer of Li_2ZrO_3 suppresses the oxygen activity by introducing strong metal–oxygen bonds at the surface of the electrode structure, which provides a diffusion pathway for the lithium ions [17–19,30]. For example, Huang et al. reported ZrO_2-coating $Li(Ni_{1/3}Co_{1/3}Mn_{1/3})O_2$ effectual to increase Li+ diffusion coefficient and reduce the active energy of interfacial Li+ transfer reaction of $Li(Ni_{1/3}Co_{1/3}Mn_{1/3})O_2$ [19].

Electrochemical impedance spectroscopy (EIS) is applied to identify the charge transfer resistance and the evolution of electrode/electrolyte interface. Fig. 8 shows the Nyquist plots of LMO and LZO-LMO electrodes carried out after the 1st and 100th cycles. The EIS curves exhibit a semicircle in the high frequency range and a sloping line in the low frequency region. The diameter of the semicircles can measure the transfer resistance (R) of the lithium-ion migration through the interface between the surface layer of the particles and the electrolyte [31]. The sloping line at the low frequency presents the diffusion process of lithium ion in the bulk of the electrode material and the Warburg resistance [32]. As shown in Fig. 8, the resistance of LMO is lower than that of LZO-LMO after the cathodes are carried out one charge/discharge cycle. It might be attributed to the fact that solid electrolyte interface grows on the surface of Li_2ZrO_3-coated LMO which results in a little increase of resistance but protects the bulk LMO in the following charge/discharge cycles at high cut-off voltage of 4.8 V. After 100 cycles, the R of LMO increases to about 12 times of the initial value, while the R of LZO-LMO increases to only less than 2 times of the initial value. It indicates that the transfer resistance and the undesirable side reaction between the cathode and electrolyte are suppressed by Li_2ZrO_3 modification.

GITT proposed by Weppner and Huggins [33] has been used as a standard method to evaluate chemical diffusion coefficients (D_{GITT}). GITT is a reliable technique to determine the chemical diffusion coefficient of lithium (D_{Li+}) with varying composition x in the cathode materials, such as Li_xMO_2 (M: transition metal element). In this work, both samples LMO and LZO-LMO as applied to a dense planar electrode have typically the same electrode thickness for the same diffusion length during charge/discharge. Fig. 9a shows the GITT curves of LMO and LZO-LMO, which samples as cathodes have been carried out for the 1st charge/discharge cycle between 2.0 and 4.8 V. The equilibrium cell voltage (E_0) will assume a new value (E_s) due to the change in Δx. As an example a single-step GITT titration at 4.38 V during the second discharge cycle of LZO-LMO, Fig. 9b shows t *vs.* E profile with schematic labeling of the relevant parameters. The cell voltage (E) decreases from the equilibrium value (E_0) with time, which is superimposed to an IR drop due to the

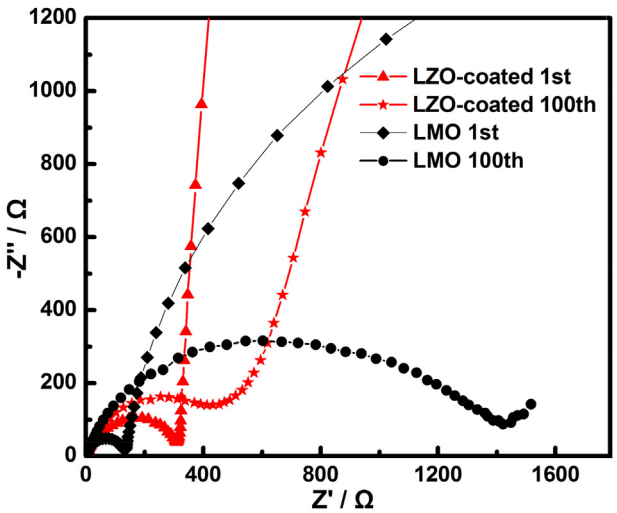

Fig. 8. Electrochemical impedance spectra of LMO and LZO-LMO after full discharge at the 1st and 100th cycles, respectively.

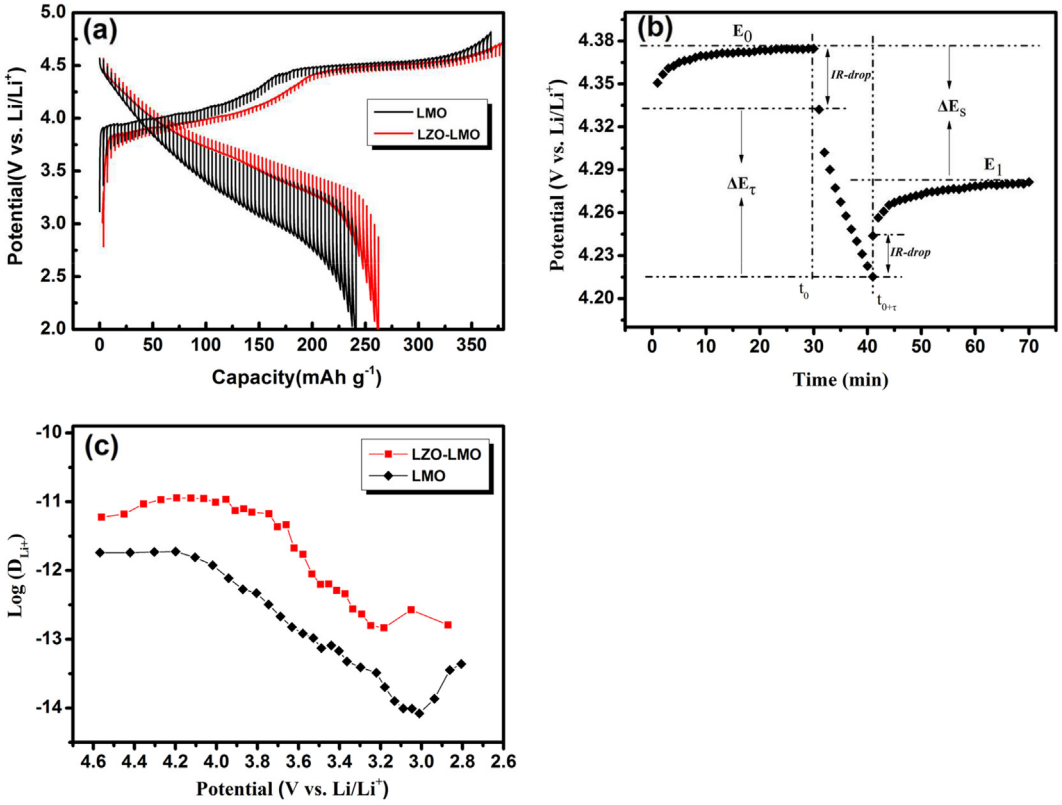

Fig. 9. (a) GITT curves of LMO and LZO-LMO between 2.0 and 4.8 V (time interval: 30 min); (b) *t vs. E* profile of LZO-LMO for a single-step GITT titration; (c) diffusion coefficients of Li^+ in LMO and LZO-LMO at different discharge states.

current flux through the electrolyte and interface [34,35]. The total change in cell voltage $\Delta E\tau$ during the current flux is obtained by subtracting the IR drops as shown in Fig. 9b. By using GITT technique, the chemical diffusion coefficients of Li^+ (D_{Li+}) shown in Fig. 9c are calculated from the potential response to a small constant current pulse via the following equation [36]:

$$D_{Li^+} = \frac{4}{\pi}\left(\frac{mV_M}{MA}\right)^2\left(\frac{\Delta E_s}{\Delta E_\tau}\right)^2 \quad (1)$$

where m (g), M ($cm^3\ mol^{-1}$) and V_M are the mass, molar mass and molar volume of active material; S ($cm^{-2}\ g^{-1}$) is the area of electrode–electrolyte interface (BET); τ (s) is the constant current pulse time; ΔE_s (V) and ΔE_τ (V) are the change of the steady-state voltage and the total change of cell voltage during a constant pulse t of a single-step GITT experiment. The sample of LMO presents the decreased D_{Li+} values along with the discharge depth, and has the lowest value of 8.34×10^{-15} $cm^2\ s^{-1}$ at 3.0 V but increases to 4.36×10^{-14} $cm^2\ s^{-1}$ at the end cut-off voltage of 2.8 V. At different voltage, the values D_{Li+} of LMO change in the range between 8.34×10^{-15} and 1.88×10^{-12} $cm^2\ s^{-1}$. The sample of LZO-LMO also presents the decreased D_{Li+} values along with the discharge depth, but has the lowest value of 1.58×10^{-13} $cm^2\ s^{-1}$ at 3.2 V and keeps a relatively stable value till the end cut-off voltage of 2.8 V. After coating with Li_2ZrO_3, the D_{Li+} values of LZO-LMO increase in the range from 1.58×10^{-13} to 1.13×10^{-11} $cm^2\ s^{-1}$. Li_2ZrO_3 coating layer enhances the Li^+ diffusion ability of LMO, for example, the D_{Li+} of LMO and LZO-LMO at 4.0 V are calculated to be 7.72×10^{-13} and 1.08×10^{-11} $cm^2\ s^{-1}$, respectively. The improvement in lithium diffusion ability of LMO after Li_2ZrO_3 coating is similar with the results in previous publications [18,37,38]. For example, Thackeray et al. synthesized the composite $0.03Li_2ZrO_3 \cdot 0.97LiMn_{0.5}Ni_{0.5}O_2$ electrodes that the improved electrochemical performance has been tentatively attributed to strong Zr–O bonds at the electrode surface and the decreased oxygen activity at the electrode surface at high potentials. Li_2ZrO_3 as lithium-ion conducting thin-film coatings are structurally compatible with close-packed metal oxide electrode substrates of LMO. Compared to the typical layered oxide such as $LiCoO_2$ (10^{-7}–10^{-11} $cm^2\ s^{-1}$) [39] and $LiNi_{1/3}Co_{1/3}Mn_{1/3}O_2$ (10^{-9}–10^{-10} $cm^2\ s^{-1}$) [40], the D_{Li+} in the LMO is much lower because of the poor conductivity and lattice disorder of Li_2MnO_3 domain. After Li_2ZrO_3 coating, the D_{Li+} values of LZO-LMO are increased and the high-rate capacity and cycle ability are improved.

4. Conclusions

In this work, $0.4Li_2MnO_3 \cdot 0.6LiNi_{1/3}Co_{1/3}Mn_{1/3}O_2$ is successfully coated with Li_2ZrO_3 via a sol–gel process. After Li_2ZrO_3 coating, LMO retains the crystal structure and lattice parameters, and particle size of LZO-LMO is similar to bare LMO. The presence of Li_2ZrO_3 effectively suppresses the resistance and improves the stability eventhough LZO-LMO carried out for 100 charge/discharge cycles. The Li^+-ion diffusion coefficient of LMO increases two orders of magnitude after Li_2ZrO_3 coating based on the results of GITT. Within the cut-off voltage of 2.5–4.8 V, LZO-LMO delivers the capacity of 264 mAh g^{-1} at 0.1 C rate, and remains 235 mAh g^{-1} after 100 cycles. At the current rates of 1, 2, 5 and 10 C, LZO-LMO delivers the capacities of 205.6, 161, 153.8 and 106 mAh g^{-1}, respectively. The Li_2ZrO_3 modification is effective to stabilize the crystal structure, increases the Li^+ diffusion ability and improves the electrochemical performance of $0.4Li_2MnO_3 \cdot 0.6LiNi_{1/3}Co_{1/3}Mn_{1/3}O_2$.

Acknowledgments

This work was financially supported in part by the 085 Project of Shanghai Education Commission, Instrumental Analysis and Research Center of Shanghai University, NSFC (_501100001809) (Grant No. 51172032).

Appendix A. Supplementary data

Supplementary data related to this article can be found at http://dx.doi.org/10.1016/j.jpowsour.2014.04.068.

References

[1] J.B. Goodenough, K.S. Park, J. Am. Chem. Soc. 135 (2013) 1167.
[2] S.-K. Hu, G.-H. Cheng, M.-Y. Cheng, B.-J. Hwang, R. Santhanam, J. Power Sources 188 (2009) 564.
[3] H.-K. Song, K.T. Lee, M.G. Kim, L.F. Nazar, J. Cho, Adv. Funct. Mater. 20 (2010) 3818.
[4] J. Park, J.H. Seo, G. Plett, W. Lu, A.M. Sastry, Electrochem. Solid-State Lett. 14 (2011) A14.
[5] M.M. Thackeray, S.H. Kang, C.S. Johnson, J.T. Vaughey, R. Benedek, S.A. Hackney, J. Mater. Chem. 17 (2007) 3112.
[6] C.R. Fell, D.H. Lee, Y.S. Meng, J.M. Gallardo-Amores, E. Moran, M.E.A. Dompablo, Energy Environ. Sci. 5 (2012) 6214.
[7] A. Ito, D. Li, Y. Sato, M. Arao, M. Watanabe, M. Hatano, H. Horie, Y. Ohsawa, J. Power Sources 195 (2010) 567.
[8] A.R. Armstrong, M. Holzapfel, P. Novak, C.S. Johnson, S.H. Kang, M.M. Thackeray, P.G. Bruce, J. Am. Chem. Soc. 128 (2006) 8694.
[9] S.H. Kang, C.S. Johnson, J.T. Vaughey, K. Amine, M.M. Thackeray, J. Electrochem. Soc. 153 (2006) A1186.
[10] C. Wu, X. Fang, X. Guo, Y. Mao, J. Ma, C. Zhao, Z. Wang, L. Chen, J. Power Sources 231 (2013) 44.
[11] Z. Wang, E. Liu, C. He, C. Shi, J. Li, N. Zhao, J. Power Sources 236 (2013) 25.
[12] D. Li, Y. Kato, K. Kobayakawa, H. Noguchi, Y. Sato, J. Power Sources 160 (2006) 1342.
[13] S.-T. Myung, K. Izumi, S. Komaba, Y.-K. Sun, H. Yashiro, N. Kumagai, Chem. Mater. 17 (2005) 3695.
[14] Y. Kim, H.S. Kim, S.W. Martin, Electrochim. Acta 52 (2006) 1316.
[15] Y.-K. Sun, Y.-S. Lee, M. Yoshio, K. Amine, Electrochem. Solid-State Lett. 5 (2002) A99.
[16] Y.L. Cheah, V. Aravindan, S. Madhavi, ACS Appl. Mater. Interfaces 5 (2013) 3475.
[17] Z. Chen, J.R. Dahn, Electrochem. Solid-State Lett. 5 (2002) A213.
[18] M.M. Thackeray, C.S. Johnson, J.S. Kim, K.C. Lauzze, J.T. Vaughey, N. Dietz, D. Abraham, S.A. Hackney, W. Zeltner, M.A. Anderson, Electrochem. Commun. 5 (2003) 752.
[19] Y. Huang, J. Chen, J. Ni, H. Zhou, X. Zhang, J. Power Sources 188 (2009) 538.
[20] H.-S. Kim, Y. Kim, S.-I. Kim, S.W. Martin, J. Power Sources 161 (2006) 623.
[21] S. Noh, J. Kim, M. Eom, D. Shin, Ceram. Int. 39 (2013) 8453.
[22] J.-H. Wang, Y. Wang, Y.-Z. Guo, Z.-Y. Ren, C.-W. Liu, J. Mater. Chem. A 1 (2013) 4879.
[23] J.S. Kim, C.S. Johnson, J.T. Vaughey, M.M. Thackeray, S.A. Hackney, W. Yoon, C.P. Grey, Chem. Mater. 16 (2004) 1996.
[24] T. Ohzuku, A. Ueda, M. Nagayama, J. Electrochem. Soc. 140 (1993) 1862.
[25] J.R. Dahn, U.V. Sacken, C.A. Michal, Solid State Ionics 44 (1990) 87.
[26] M.M. Thackeray, S.H. Kang, C.S. Johnson, J.T. Vaughey, S.A. Hackney, Electrochem. Commun. 8 (2006) 1531.
[27] C.W. Park, I. Ruth Mangani, H.W. Ryu, C.J. Park, J.S. Lee, S.J. Song, J.H. Moon, J. Kim, J. Phys. Chem. Solids 68 (2007) 1126.
[28] M.M. Thackeray, C.S. Johnson, J.T. Vaughey, N. Li, S.A. Hackney, J. Mater. Chem. 15 (2005) 2257.
[29] C.S. Johnson, N. Li, C. Lefief, J.T. Vaughey, M.M. Thackeray, Chem. Mater. 20 (2008) 6095.
[30] J. Cho, T.-J. Kim, Y.J. Kim, B. Park, Angew. Chem. Int. Ed. 40 (2001) 3367.
[31] S.K. Martha, J. Nanda, G.M. Veith, N.J. Dudney, J. Power Sources 199 (2012) 220.
[32] S.J. Shi, J.P. Tu, Y.Y. Tang, Y.X. Yu, Y.Q. Zhang, X.L. Wang, J. Power Sources 221 (2013) 300.
[33] W. Weppner, R.A. Huggins, J. Electrochem. Soc. 124 (1977) 1569.
[34] K.M. Shaju, G.V.S. Rao, B.V.R. Chowdari, Electrochim. Acta 48 (2003) 2691.
[35] S.J. Shi, J.P. Tu, Y.Y. Tang, Y.Q. Zhang, X.L. Wang, C.D. Gu, J. Power Sources 240 (2013) 140.
[36] E. Deiss, Electrochim. Acta 50 (2005) 2927.
[37] J.F. Ni, H.H. Zhou, J.T. Chen, X.X. Zhang, Electrochim. Acta 53 (2008) 3075.
[38] C.G. Wang, L. Chen, H. Zhang, Y. Yang, F. Wang, F. Yina, G. Yang, Electrochim. Acta 119 (2014) 236.
[39] M. Park, X.C. Zhang, M. Chung, G.B. Less, A.M. Sastry, J. Power Sources 195 (2010) 7904.
[40] K.M. Shaju, G.V.S. Rao, B.V.R. Chowdariz, J. Electrochem. Soc. 151 (2004) A1324.